OPTICS

Tackling light trapping in organic light-emitting diodes by complete elimination of waveguide modes

Changyeong Jeong†, Yong-Bum Park†, L. Jay Guo*

Copyright © 2021 The Authors, some rights reserved; exclusive licensee American Association for the Advancement of Science. No claim to original U.S. Government Works. Distributed under a Creative Commons Attribution NonCommercial License 4.0 (CC BY-NC).

Conventional waveguide mode decoupling methods for organic light-emitting diodes (OLEDs) are typically not scalable and increase fabrication complexity/cost. Indium-tin-oxide–free transparent anode technologies showed efficiency improvement without affecting other device properties. However, previous works lack rigorous analysis to understand the efficiency improvement. Here, we introduced an ultrathin silver (Ag) film as transparent electrode and conducted systematic modal analysis of OLEDs and report that waveguide mode can be completely eliminated by designing an OLED structure that is below the cutoff thickness of waveguide modes. We also experimentally verified the waveguide mode removal in organic waveguides with the help of index-matching fluid and prism. The negative permittivity, extremely thin thickness (~5 nanometers), and highly conductive properties achieved by a uniform copper-seeded Ag film can suppress waveguide mode formation, enhancing external quantum efficiency without compromising any other characteristics of OLEDs, which paves the way for cost-effective high-efficiency OLEDs in current display industry.

INTRODUCTION

Recently, organic light-emitting diodes (OLEDs) have taken the center stage as emitting cells for flexible and transparent displays, thanks to their excellent flexibility, aesthetics, low production cost, and great compatibility with other optoelectronic devices (*1*, *2*). OLEDs have successfully achieved 100% internal quantum efficiency (IQE) with the help of phosphorescent molecules containing metal complex (*3*) and thermally activated delayed fluorescence molecules with small singlet and triplet energy gap (*4*), proving its great potential for future energy-efficient displays in daily lives. However, the external quantum efficiency (EQE) of OLEDs is limited to around 20% without any outcoupling structure on a glass substrate, which needs to be addressed to realize its full potential (*5*–*7*). Therefore, searching for solutions to effectively liberate the light trapped inside the device is one of the most important and urgent tasks in OLED research area today.

There are three major factors that limit EQE of OLEDs (*6*, *7*). First, a portion of generated photons from the emissive layer (EML) is lost at the interface between contact metal and organic stacks due to the excitation of surface plasmon-polariton (SPP) mode. Second, light is trapped in the substrate and cannot escape a device due to total internal reflection at the air/substrate interface. Third, light generated at the EML is trapped inside the OLED as propagating mode since organic stacks and transparent conducting electrode (TCE) act as a waveguide. There have been extensive research to extract trapped light at the substrate, and practical solutions are now available, but liberating light that is trapped and lost in the SPP and waveguide modes remains a challenge. In particular, the SPP mode is inevitably created by the use of contact metal necessary for the OLED, and the energy rapidly dissipates as heat, representing an unrecoverable energy loss. One effective solution to avoid such energy loss is to use a thick electron transport layer (ETL) (*6*, *8*), where the energy dissipated to SPP is substantially reduced, but a larger portion of the light energy resides in the waveguide mode. In addition, recent work showed that the electrical characteristic of OLEDs is not compromised with an extremely thick ETL when perovskite materials are used for ETL, thus potentially addressing the reduction of the SPP loss in OLEDs (*9*). In this case, the final frontier in reaching high EQE is to free the light trapped in the waveguide.

Previously, several strategies were introduced to outcouple light trapped in the waveguide mode by inserting low-index grids (*10*), gratings (*11*), buckling patterns (*12*), reactive ion etching–induced nanostructure (*13*), or corrugated structures (*14*) in OLEDs. However, these approaches are either wavelength dependent due to the existence of coupling resonance or intrusive to the OLED structure. Some require complex fabrication steps that increase not only cost but also incompatibility with large-area manufacturing processes. Therefore, there is a strong need for a new approach to solve the waveguide problem that is nonintrusive, simple to fabricate, easily scalable, cost-effective, wavelength independent, and compatible with large-area OLED fabrication processes. Such a solution, if developed, can lead to energy-efficient OLEDs (as well as other LEDs) and can have immediate impact on commercial display products.

Thin-film electrode technologies are preferred to achieve this goal as it only involves film deposition, compatible with OLED fabrication process. There are several reports of improved outcoupling efficiency of OLEDs by simply replacing indium tin oxide (ITO) with the emerging TCEs such as carbon-based materials (*15*–*17*), conductive polymers (*8*, *18*, *19*), or metal-based materials (*20*–*22*). In particular, OLED using conductive poly(3,4-ethylenedioxythiophene): poly(styrenesulfonate) (PEDOT:PSS) as an anode (*8*, *19*) reached a maximum EQE of 64.5% due to its lower refractive index than ITO. However, the conductivity of PEDOT:PSS is too low for practical OLED operation, and complex postprocessing (*23*–*25*) is required to improve its conductivity. Graphene electrode was also engineered to demonstrate efficiency improvement and showed that device EQE can reach 64.7% with optimized PEDOT:PSS and titanium dioxide around the graphene layer (*17*). However, considering that the sheet resistance (R_{sh}) of graphene needs to be lower than at least 100 ohms/sq for OLED applications (*26*) and R_{sh} < 20 ohms/sq for flat panel displays (*27*), the high R_{sh} value of pristine graphene

Department of Electrical Engineering and Computer Science, University of Michigan, Ann Arbor, MI 48109, USA.
*Corresponding author. Email: guo@umich.edu
†These authors contributed equally to this work.

(R_{sh} > 300 ohms/sq) requires special doping process but lacks long-term stability. Still, the production cost of high-quality large-area graphene films remains high for practical use for OLEDs (*25*). In comparison, semitransparent ultrathin metal films by simple physical vapor deposition (PVD) are promising candidates in terms of high conductivity, reliable fabrication process, and compatibility with display manufacturing processes. The ultrathin metal film can also help light outcoupling efficiency. Previous reports showed that gold on photoresist film (*21*) or Ag alloys (*22*) can suppress mode guided by the high-index ITO, enhancing device efficiency compared to the ITO device by ~25%. However, these studies were unable to provide a comprehensive analysis to unravel the mechanism behind the enhanced outcoupling efficiency.

In this work, we systematically investigate the light power distribution in ultrathin Ag film–based OLEDs. We report that the waveguide mode can be completely eliminated by optimizing the organic stacks and the ultrathin Ag anode. To the best of our knowledge, this is the first systematic study by detailed analysis and to experimentally demonstrate the complete removal of waveguide mode by using thin-film electrode technology. This simple yet effective method is compatible with the commonly used fabrication process and enhances the EQE of OLEDs without compromising other device characteristics. Our modal analysis reveals the mechanism for eliminating the waveguide mode: The intrinsic negative permittivity nature and extremely thin thickness of the Ag anode bring the waveguide modes below its cutoff thickness. Therefore, the normal organic layer thickness used in OLEDs does not support the waveguide modes, leading to notably enhanced EQE. We successfully fabricated an ultrathin uniform Ag film of around 5 nm using copper (Cu) seed layer (will be referred to as Cu-Ag) that has R_{sh} = 21.3 ohms/sq and transmittance at λ = 550 nm (T_{550}) of 80.7%. We designed an experiment to prove the absence of the guided modes in an organic waveguide with the thin Cu-Ag film (*28*). The in-depth analysis conducted in this work enlightens the underlying principle attributed to the improved EQEs of the thin metal film–based OLEDs, and the solution suggested in this work directly addresses the root cause of waveguide mode in OLEDs, which can have an immediate impact on commercial products in the industry. The mode removal mechanism introduced in this work helps explain the mechanism of the increased light output efficiency in the previously reported ITO-free OLEDs (*8*, *15*, *16*, *18*, *20*–*22*, *28*–*30*). Our solution is not only simple in process but also can achieve high throughput and low cost with excellent compatibility with the large-scale manufacturing process in display industry. In principle, the modal elimination approach introduced in this work could be extended to other solid-state LEDs such as perovskites (*31*), quantum dots (*32*), or III-V–based LEDs (*33*) since all of which are susceptible to the issue of light trapping as waveguide mode.

RESULTS AND DISCUSSION

Theoretical investigation of waveguide mode elimination

Light generated at the active region excites the SPP and waveguide modes (*6*), where the SPP mode is the fundamental transverse magnetic (TM_0) mode and the waveguide modes consist of the fundamental transverse electric (TE_0) and first-order TM (TM_1) modes. The fundamental TM_0 mode, SPP mode, is always excited when the metal cathode is in close proximity to the dipole emitters, as is the case in an OLED structure. On the other hand, the two waveguide modes, TE_0 and TM_1 modes, can experience modal cutoff under certain conditions. When such conditions are satisfied, they no longer exist in OLEDs, thereby eliminating the light trapping within the device. In this section, we will show that such conditions can be easily satisfied by using an ultrathin Ag anode that replaces the conventional ITO electrode.

To investigate the behaviors of the two waveguide modes, TE_0 and TM_1 modes, its eigenvalue equations were derived by solving Maxwell's equations in a multilayer waveguide geometry (*34*, *35*). Derivations of the eigenvalue equations are detailed in section S1. The waveguide consists of aluminum (Al) cathode/organic layer/150-nm ITO or 5-nm Cu-Ag anode/glass substrate as shown in Fig. 1A, along with the field profiles of the calculated TE_0 and TM_1 modes, where 4,4′-bis(*N*-carbazolyl)-1,1′-biphenyl (CBP) was used for the organic layer. Here, to simplify the modal calculation without losing generality, we assumed that the ETL and hole transport layer (HTL) have the same index as EML. Characteristics and fabrication of the ultrathin Cu-Ag film are discussed in Fig. 2 and section S3. The effective indices of the two waveguide modes ($n_{eff,TE0}$ and $n_{eff,TM1}$) were obtained as functions of organic layer thickness ($t_{organic}$) at the emission wavelength of 530 nm and plotted in Fig. 1 (B and C, respectively). For a given organic thickness, each waveguide mode is characterized by its effective index, and the higher $n_{eff,TE0}$ or $n_{eff,TM1}$

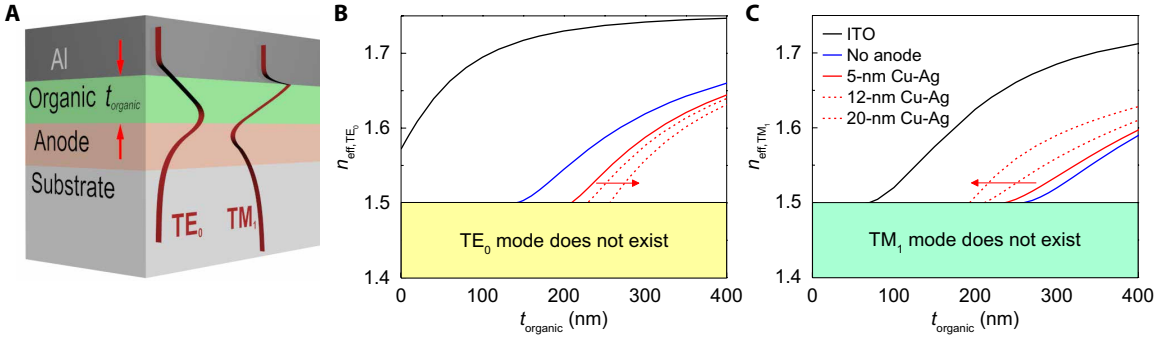

Fig. 1. Theoretical investigation of waveguide mode elimination. (**A**) Schematic illustration of the calculated waveguide structure. Electric field of TE_0 mode and magnetic field of TM_1 mode are also depicted. Calculated effective indices of (**B**) TE_0 ($n_{eff,TE0}$) and (**C**) TM_1 ($n_{eff,TM1}$) modes as functions of organic layer thickness $t_{organic}$. Devices without anode (blue) and with anode of Cu-Ag of varying thickness (red, solid or dotted lines) or ITO (black) were calculated. Introduction of the Cu-Ag film increases the cutoff thickness, meaning that the Cu-Ag film prevents the formation of the waveguide mode. Arrow in each figure shows the direction of increase in Cu-Ag film thickness.

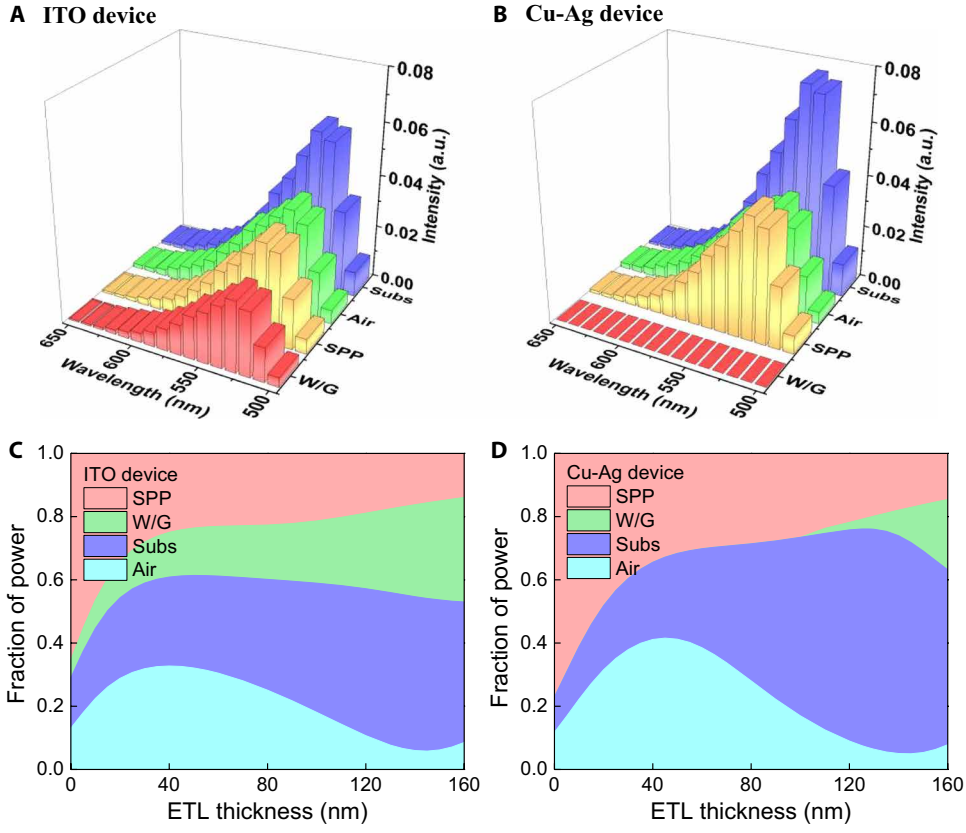

Fig. 2. Model power distribution. Spectral power distribution of each mode in (**A**) ITO and (**B**) Cu-Ag OLEDs. a.u., arbitrary units. Intensity at 530 nm is the highest as it is the peak emission wavelength of $Ir(ppy)_2acac$. Fractions of Air, Subs, W/G, and SPP are referred to the energy transferred to the air, glass, waveguide, and SPP modes, respectively. Waveguide mode was removed in the Cu-Ag device, showing zero intensity. Power distribution of each mode as functions of ETL thickness in (**C**) ITO and (**D**) Cu-Ag OLEDs. Extractable light portion (Air + Subs) increases in the Cu-Ag device due to waveguide mode elimination. Waveguide mode starts to appear in the Cu-Ag OLED at thick ETL.

is, the stronger the modal confinement, indicating that both the TE_0 and TM_1 modes are more tightly confined in the waveguide with the ITO anode. The guided mode with smaller $n_{eff,TE0}$ or $n_{eff,TM1}$ is more loosely confined and even no longer supported in the waveguide when $n_{eff,TE0}$ or $n_{eff,TM1}$ becomes lower than the refractive index of the glass substrate, n_{glass} = 1.5. This sets the condition for the cutoff thickness of each mode as depicted in Fig. 1 (B and C). The ultrathin Cu-Ag film as an anode eliminates both TE_0 and TM_1 modes when the organic stack is less than ~200 nm. Such a condition can be easily satisfied by using typical OLED materials and structures and by simply replacing the conventional ITO electrode with the thin transparent Cu-Ag.

The mechanism responsible for the elimination is different for TE_0 and TM_1 modes. TE_0 mode is a purely dielectric mode (i.e., index guiding) that is guided by the refractive index difference between the core and clad of the waveguide. The core of the waveguide is organic stack and anode, whereas the clad is Al and the glass substrate. The blue curve in Fig. 1B shows the effective index of TE_0 mode when only the organic stack acts as a waveguide core without any anode (no anode). Because of the large geometric/optical asymmetry and semi-infinite metallic clad of the waveguide, the TE fundamental mode experiences intrinsic mode cutoff at $t_{organic}$ = 140 nm. The insertion of a 150-nm ITO increases the modal confinement of the TE mode and reduces the cutoff thickness of the organic stack. This leads to the well-known fact that TE mode is always guided in ITO-based OLEDs as $n_{eff,TE0}$ is higher than n_{glass} even at $t_{organic}$ = 0. In contrast, the large negative permittivity of the thin Cu-Ag anode at visible wavelength, $Re(\varepsilon_{Cu\text{-}Ag}) \sim -10$, played a substantial role in reducing the effective refractive index of the core and thus reducing the modal confinement of the mode (red curves). The reduced $n_{eff,TE0}$ greatly relaxes the cutoff condition, where the cutoff organic stack thicknesses increase to 208, 243, and 256 nm for 5-, 12-, and 20-nm Cu-Ag films, respectively. Therefore, for a typical organic stack thickness of 100 to 200 nm in OLEDs, the thin Cu-Ag film can effectively suppress the formation of TE mode, which can never be achieved by other types of TCEs having high index values. The figure also shows that a thicker Cu-Ag film further reduces $n_{eff,TE0}$ and increases the cutoff thickness of the organic stack, but as will be discussed later, there is an optimal thickness to achieve high EQE.

Unlike the pure index guiding nature of TE mode, TM mode has a plasmonic nature with its electric field perpendicular to the material stack and thus can be efficiently guided in the presence of metal (*36*, *37*). The TM_1 modal cutoff solely depends on the total thickness of the waveguide; therefore, replacing the thick ITO anode with the ultrathin Cu-Ag film reduces the waveguide thickness to below the TM_1 mode cutoff value. It means that the extremely thin nature of the Cu-Ag film suppresses the formation of the TM_1

waveguide mode. Since TM_1 mode is a higher-order mode, it has a larger cutoff thickness compared to the fundamental mode, showing the cutoff thickness at $t_{organic}$ = 259 and 69 nm for the no-anode and ITO devices and $t_{organic}$ = 236, 211, and 193 nm for 5-, 12-, and 20-nm-thick Cu-Ag devices, respectively. One can see that unlike the TE_0 case, TM_1 mode cutoff is also possible in the ITO device when $t_{organic}$ < 70 nm. However, this thickness is much lower than the practical $t_{organic}$ value that lies in the range of 100 to 200 nm in typical OLEDs, making it unrealistic in OLEDs. In comparison, the TM_1 mode is not supported up to $t_{organic}$ = 236 nm in the thin Cu-Ag device, which means that for the practical organic stack thickness, TM_1 mode is also eliminated in such devices. The insertion of the 5-nm Cu-Ag film has little change in the cutoff thickness as compared to the no-anode device. The elimination of the TM_1 mode can hardly be achieved by metal oxide–based TCEs such as ITO and IZO as reducing its thickness will make it too resistive to be practical. More detailed mathematical and physical mechanisms of the waveguide mode elimination are explained in section S1.

Modal power distribution in OLEDs

Optical property of OLEDs with the thin Cu-Ag anode is investigated and compared to that with ITO anode in this section. Here, we used a typical organic structure for the calculation, which is the same as the organic waveguide investigated in the previous section but the dielectric core was substituted by an archetypical organic stack consisting of 5-nm molybdenum trioxide (MoO_3)/40-nm di-(4-(*N*,*N*-di-*p*-tolyl-amino)-phenyl) cyclohexane (TAPC)/20-nm EML/75-nm 1,3,5-tris(1-phenyl-1*H*-benzimidazol-2-yl)benzene (TPBi), where CBP was used for the EML in the calculation. Figure 2 (A and B) shows the spectral power distribution of each mode in the ITO- and thin Cu-Ag–based OLEDs, respectively, which was calculated by dyadic Green's function (see Materials and Methods) (*38*). W/G, SPP, Air, and Subs are referred to as waveguide, SPP, air, and substrate modes, respectively, and the total power was normalized to unity, assuming the ideal case of IQE = 100%. The power distribution shows the highest power at 530 nm, which is the peak wavelength of the emitter used in this work, bis(2-(2-pyridinyl-*N*)phenyl-C)(2,4-pentanedionato-O2,O4)iridium(III) [$Ir(ppy)_2acac$]. The ITO device showed relatively similar amount of the power distributed in each mode, with the highest fraction at the substrate mode. In contrast, in the Cu-Ag device, the waveguide mode has completely disappeared within the entire wavelength range, where the suppressed power was distributed to the other modes, leading to the increased power as compared to the ITO device. Among them, the substrate mode showed the largest increase, meaning that the energy corresponding to the waveguide mode is transferred to the substrate with the largest amount and relatively small portion to air and metal.

The fraction of power distributed in each optical mode in the ITO and Cu-Ag devices was calculated as functions of ETL thickness in Fig. 2 (C and D), where hole injection layer (HIL), HTL, and EML in both devices were fixed to 5, 40, and 20 nm, respectively. The calculation showed that the Cu-Ag device has a higher maximum air mode portion reaching 41.5%, whereas it is 32.7% for the ITO device. The substrate mode portion notably increased in the Cu-Ag device, and the enhancement of the substrate mode is more noticeable with a thicker ETL. As reported previously, a thick ETL reduces SPP mode portion while increasing waveguide mode in conventional OLEDs (*6*). However, in the Cu-Ag device, the thick ETL largely increases the substrate mode portion with negligible waveguide mode. The calculation showed that the maximum achievable EQE of the Cu-Ag OLED is 76.1% from the sum of the air and substrate modes that are easily extracted, whereas that of the ITO device can only reach 61.4%, showing a 14.5% EQE improvement by introducing the ultrathin Cu-Ag film. Therefore, the use of a 5-nm-thin Cu-Ag anode suppresses the formation of waveguide modes in OLEDs and transfers its corresponding energy to the air and the substrate mode that can be extracted as useful light emission. Air mode fraction is very small when the extractable energy portion (Air + Subs) is very large (ETL = 130 nm). Therefore, the Cu-Ag OLED structure should be designed on the basis of an application and the mode to be extracted. If a geometry does not need substrate mode extraction, then it is more favorable to design a Cu-Ag OLED with ETL = 45 nm for the largest air mode extraction. At ETL = 75 nm calculated for Fig. 2 (A and B), the ITO device showed 16.0% of the total power in the waveguide mode, which eventually

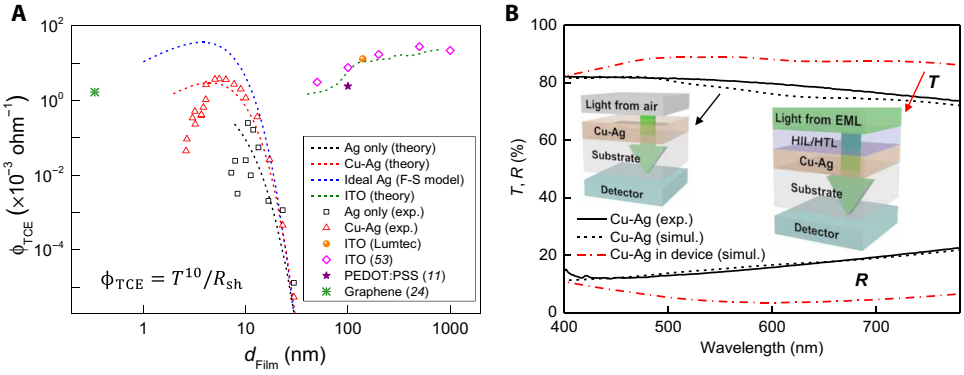

Fig. 3. Electrical and optical properties of Cu-Ag transparent conductor. (**A**) Haacke's figure-of-merit ϕ_{TCE} as a function of film thickness for Cu-Ag, Ag-only, ITO-, PEDOT:PSS-, and graphene-based transparent conductors. Experimental data (in symbol) and simulated data (dotted line) of Ag-only film (black) and Cu-Ag film (red) are plotted together. Theoretical ϕ_{TCE} of an ideal Ag film is also plotted (blue dotted line) to show the potential of the metal film–based TCE. Models used for the calculated curves can be found in section S2. (**B**) Measured (black solid line) and simulated (black dashed line) transmittance (*T*) and reflectance (*R*) of Cu-Ag films in air. Simulated *T* and *R* values of Cu-Ag films inside an OLED structure are also plotted (red dashed line) showing enhancement of transmittance owing to the AR effect of the HIL/HTL layer. Schematics of the simulated optical stacks are illustrated in inset for each curve.

dissipates. In contrast, no power was distributed to the waveguide mode in the Cu-Ag device but instead redistributed to the air, glass, and SPP modes, respectively. In particular, the substrate mode receives the largest portion.

It is worth mentioning that the efficiency improvement due to the waveguide mode elimination by Cu-Ag becomes slightly larger when $Ir(ppy)_2acac$ is replaced with $Ir(ppy)_3$ that has an isotropic emitter dipole orientation. This can be understood because vertically oriented dipoles (which accounts for one-third of the isotropic dipoles) excite larger amount of SPP and TM_1 modes than that with horizontal orientation, resulting in smaller EQEs for both ITO and Cu-Ag OLEDs. However, because of the higher waveguide mode portion from the isotropic dipole source, the efficiency difference between the ITO and Cu-Ag OLEDs becomes larger. With a very large horizontal dipole factor, the ITO device already emits large amount of light to glass and air, with less effect of waveguide mode outcoupling.

Fabrication of extremely thin Cu-Ag film for OLEDs

To maximize the effect of the waveguide mode removal and achieve high EQE of OLEDs, Cu-Ag anode should be extremely thin and have low optical loss. Thicker Cu-Ag layer can reduce light transmission through the anode and increase microcavity effect that leads to the undesirable angle-dependent emission spectra. The key to a metal film–based TCE lies in controlling its thickness well below the optical skin depth (~20 nm for Ag at 530 nm) to achieve high light transmission (*39*). Ag is ideal for this purpose because of its high electrical conductivity and low optical loss at visible wavelength. However, a thin Ag film is prone to grow in three-dimensional (3D) island-like (Volmer-Weber) modes on oxide substrates, leading to high electrical resistance and optical scattering loss (*40*). Inorganic seed layers such as germanium (Ge), Cu, and Al are very effective in promoting Ag wetting and suppress island-like growth, thereby enabling an ultrathin smooth film with low optical loss (*41*–*43*). Ge, Cu, and Al seed layers were compared on the basis of film roughness, binding strength energy, electrical resistivity, transmittance (T) of Ag films on these layers, and film stability, where the best performance was observed with a 5-Å Cu seed layer (see section S3). The readers can refer to a recent review article on thin metal film–based transparent conductors (*44*).

In choosing the optimum thickness condition of Ag film for TCE, Haacke's figure of merit [$\phi_{TCE} = (T_{550})^{10}/R_{sh}$] was calculated for varying film thickness (d_{film}) (*45*). Figure 3A shows the measured and calculated ϕ_{TCE} of high-performance TCEs (Cu-Ag, bare Ag, PEDOT:PSS, graphene, and ITO films) as a function of d_{film}. Note that substantial improvement in ϕ_{TCE} was observed with the aid of only a 5-Å Cu, where the value reached maximum at d_{film} = 5.0 nm with T_{550} = 80.7% and R_{sh} = 21.3 ohms/sq, which was chosen as the optimum Ag thickness in this work. ϕ_{TCE} of the state-of-the-art ITOs (*46*) including commercial ITO (Luminescence Technology Corporation) calculated from transfer-matrix method (*47*) and grain-boundary scattering (*48*) is also plotted in Fig. 3A for comparison. ϕ_{TCE} of the commercial ITO (R_{sh} = 15 ohms/sq and T_{550} = 85.0%) is higher than that of the fabricated Cu-Ag film but lower than that of the ideal Ag film, which only considers surface scattering, indicating that the Ag film with improved film quality can surpass the performance of ITO as TCE. Postprocessed PEDOT:PSS and graphene also showed comparable ϕ_{TCE} to Cu-Ag but did not reach the performance of the ideal Ag films. Since both high ϕ_{TCE} and extremely thin thickness of TCEs contribute to better outcoupling of OLEDs, TCEs located at the top left in Fig. 3A are expected to bring higher device performances when they are used in OLEDs. Theoretical calculation of ϕ_{TCE} for Ag and ITO films based on corresponding resistivity models is discussed in section S4.

The extremely thin Cu-Ag film was highly transparent, reaching measured T_{550} of 80.7% and reflectance at λ = 550 nm (R_{550}) of 14.2%. This optical property can be further enhanced by HTL and HIL in OLEDs directly adjacent to the anode, which function as antireflective (AR) layers. Figure 3B shows the calculated T value and reflectance (R) of 5-nm Cu-Ag films on a glass substrate (black dashed line) and embedded in an OLED structure as an anode (red dashed dots), where light was incident from the top of the structures as shown in the insets of Fig. 3B. CBP, TAPC, and MoO_3 were used for EML, HTL, and HIL, respectively. TAPC and MoO_3 were fixed to 50 and 5 nm, respectively, and acted as effective AR coatings for

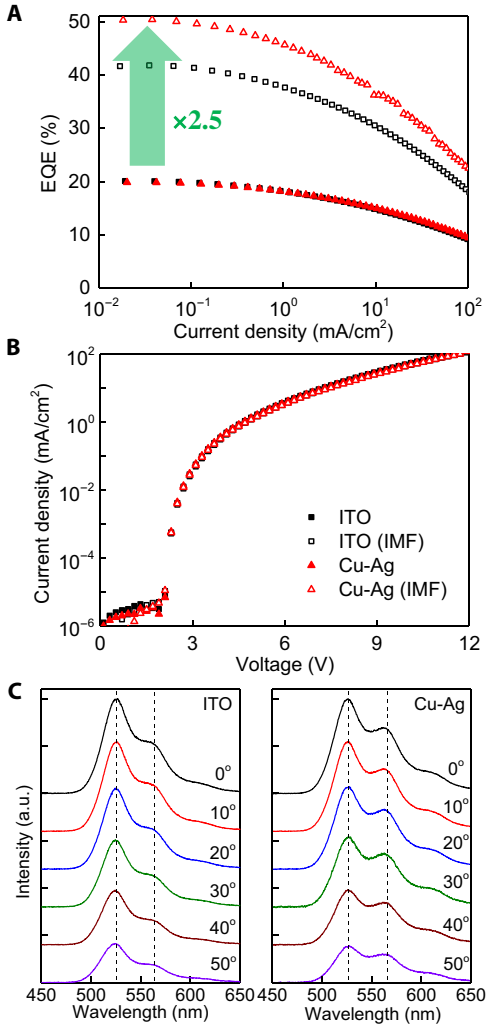

Fig. 4. Device performance of Cu-Ag and ITO-based OLEDs. (**A**) EQE–current density and (**B**) current density–voltage characteristics of Cu-Ag and ITO OLEDs with and without IMF. IMF was used to extract the light trapped in the substrate. (**C**) Measured spectra of the ITO and Cu-Ag OLEDs at angles from 0° to 50°. Both devices showed angle-insensitive emission spectra. Vertical dotted lines in each graph indicate the peak position of the emission spectrum.

the Cu-Ag film. The calculation showed that simulated R_{550} is suppressed from 15.2 to 4.0% (i.e., to a level similar to that of the substrate) and simulated T_{550} is enhanced from 78.4 to 88.9%, indicating the effectiveness of the AR effect from the HIL/HTL. *T* value can reach 88.8% at λ = 530 nm, which is the peak emission wavelength of $Ir(ppy)_2acac$. Permittivity of the fabricated Cu-Ag film used for the calculation in this work is represented in section S4.

OLED performances

A green OLED based on a conventional structure (*49*) was fabricated with either ITO or Cu-Ag anode to observe the effect of the waveguide mode removal on the device outcoupling efficiency. Fabricated OLEDs consist of glass substrate/150-nm ITO or 5-nm Cu-Ag/5-nm MoO_3/40-nm TAPC/20-nm 10% $Ir(ppy)_2acac$ doped in CBP/75-nm TPBi/1.5-nm LiQ/150-nm Al, where OLEDs with ITO anode serves as a reference. Figure 4A shows the measured EQE versus current density characteristic of each device. EQEs of the ITO and Cu-Ag devices were 20.2 and 19.9%, respectively, which are a similar fraction to the calculated air mode portion shown in Fig. 2 (C and D). However, the Cu-Ag device shows a slightly lower EQE than the ITO device since the 5-nm Cu-Ag film creates 5% photon absorption loss as shown in fig. S6. The measured EQEs of both the devices were lower than the calculated values because the IQE of the fabricated device is less than 100% assumed for the calculation in Fig. 2 (C and D). The fabricated OLEDs in this work are likely to experience exciton quenching due to triplet-triplet and triplet-polaron annihilations especially at the EML and ETL interface since CBP and $Ir(ppy)_2acac$ both transport holes more favorably than electrons (*50*, *51*). Also, exciton loss happens since organic semiconductors used in the fabrication were used as received without further purification. Considering these exciton losses, the IQE of the fabricated devices was about 77%. The most straightforward method to extract the trapped light in the substrate is the use of index-matching fluid (IMF). Therefore, IMF was used to extract the substrate mode and observe the waveguide mode elimination effect. In practice, microlens array or other patterned structures can be used to achieve a similar effect (*52*). The EQE of the Cu-Ag device notably increased to 50.6% with the substrate mode extraction, whereas that of the ITO device remains at a maximum of 42.3% as shown in Fig. 4A. This efficiency improvement due to the substrate mode extraction showed the same trend with Fig. 2 (C and D) under the assumption of IQE = 77%. It further testifies that the Cu-Ag device has a larger portion of light residing in the substrate due to the elimination of the waveguide mode in the OLED. Table 1 summarizes the calculated and measured fraction of each mode, where Air mode corresponds to EQE without IMF and the sum of Air and Subs fractions is EQE with the substrate mode extraction.

Bottom-emitting OLEDs were fabricated in this work with IMF under the device to extract the substrate mode. Recently, there is a great deal of attention in top-emitting OLEDs in the industry that do not suffer from substrate loss. In such a structure, light extraction becomes more straightforward since the generated light can directly escape the device without the need of substrate mode extraction. Formation of waveguide mode is also suppressed in top-emitting OLEDs when Ag alloy is used for TCE. From a waveguide point of view, glass clad is replaced with air in top-emitting OLEDs, which increases the refractive index difference between the waveguide core and clad, thus requiring thinner organic waveguide to achieve the waveguide mode cutoff.

Figure 4B shows the measured current density–voltage characteristic of the ITO and Cu-Ag devices. The two devices showed very similar electrical properties, overlapping in the curves. This indicates that the electrical property of OLEDs was unaltered by replacing ITO with Cu-Ag. Therefore, the EQE enhancement from Cu-Ag is purely an optical effect and the result of more emitted photons being coupled out of the OLEDs. Due to the low reflectivity of the Cu-Ag film with AR coating, the OLEDs with Cu-Ag showed angle-insensitive emission color without strong cavity effect, as evidenced by the spectra of the Cu-Ag OLEDs measured at oblique angles from 0° to 50° in Fig. 4C. The emission profile of the Cu-Ag device is very similar to that of the ITO device, which has a Lambertian profile (see section S6).

Table 1. Calculated and measured fraction (in percentage) of each mode in ITO and Cu-Ag OLEDs. Maximum EQEs are denoted for measured ITO and Cu-Ag. Values in parenthesis were obtained with the assumption IQE = 77%.

Mode	Calculated ITO	Calculated Cu-Ag	Measured ITO	Measured Cu-Ag
Air	26.3 (20.3)	27.7 (21.3)	20.2	19.9
Subs	35.1 (27.0)	43.8 (33.7)	22.1	30.7
Waveguide	16.0 (12.3)	0 (0)	–	–
SPP	22.6 (17.4)	28.8 (21.9)	–	–

Table 2. Summary of the selected high-performance ITO-free OLEDs.

Anode	R_{sh} (ohms/sq)	Control device EQE (%)*	Improved device EQE (%)†	Enhancement factor‡	Reference
Cu-Ag	21.3	20.2	50.6	2.5	This work
PEDOT:PSS	145	26.4	64.5	2.4	(*8*)
PEDOT:PSS	145	23.1	44.1	1.9	(*18*)
PEDOT:PSS	150	14.1	17.2	1.2	(*19*)
Graphene	92.5	27.4	64.7	2.4	(*17*)

*Control EQE is the maximum EQE of the ITO reference sample on the flat glass substrate. †Improved EQE is the maximum EQE of the suggested structure with the substrate mode outcoupling. ‡Enhancement factor is the ratio between the control and improved EQEs.

The Cu-Ag OLED studied in this work was compared with the selected high-performance ITO-free OLEDs in Table 2. Device efficiency and R_{sh} value of an anode both are critical aspects for practical OLED applications, especially for large-area products; therefore, both factors were compared in Table 2. Enhancement factor, which is the ratio to the light output of an ITO reference sample (*53*), was used to characterize the improved light extraction efficiency. It showed that Cu-Ag can achieve the highest enhancement factor of 2.5 in OLEDs and the lowest R_{sh} value. The enhancement factor was similar to that of the PEDOT:PSS- and graphene-based OLEDs, but the R_{sh} value of Cu-Ag was substantially lower than that of PEDOT:PSS and graphene, showing the great potential of Cu-Ag for future display applications. Also, Cu-Ag only needs a simple PVD process that is already widely used in the industry, which will deliver the direct and immediate impact on the industry among other ITO-free candidates.

Observation of waveguide mode elimination

To provide a further direct experimental verification of the waveguide mode elimination, we prepared organic waveguide samples grown on the ITO and Cu-Ag films. Strip-line organic layers with commercial ITO on a glass substrate and sputtered Cu-Ag on a fused silica substrate were prepared. The organic waveguide structure was 30-nm TAPC/20-nm 8% $Ir(ppy)_2acac$ doped in CBP/40-nm ETL, but without the top Al layer, to allow a more accurate measurement of waveguide mode intensity because the Al cladding

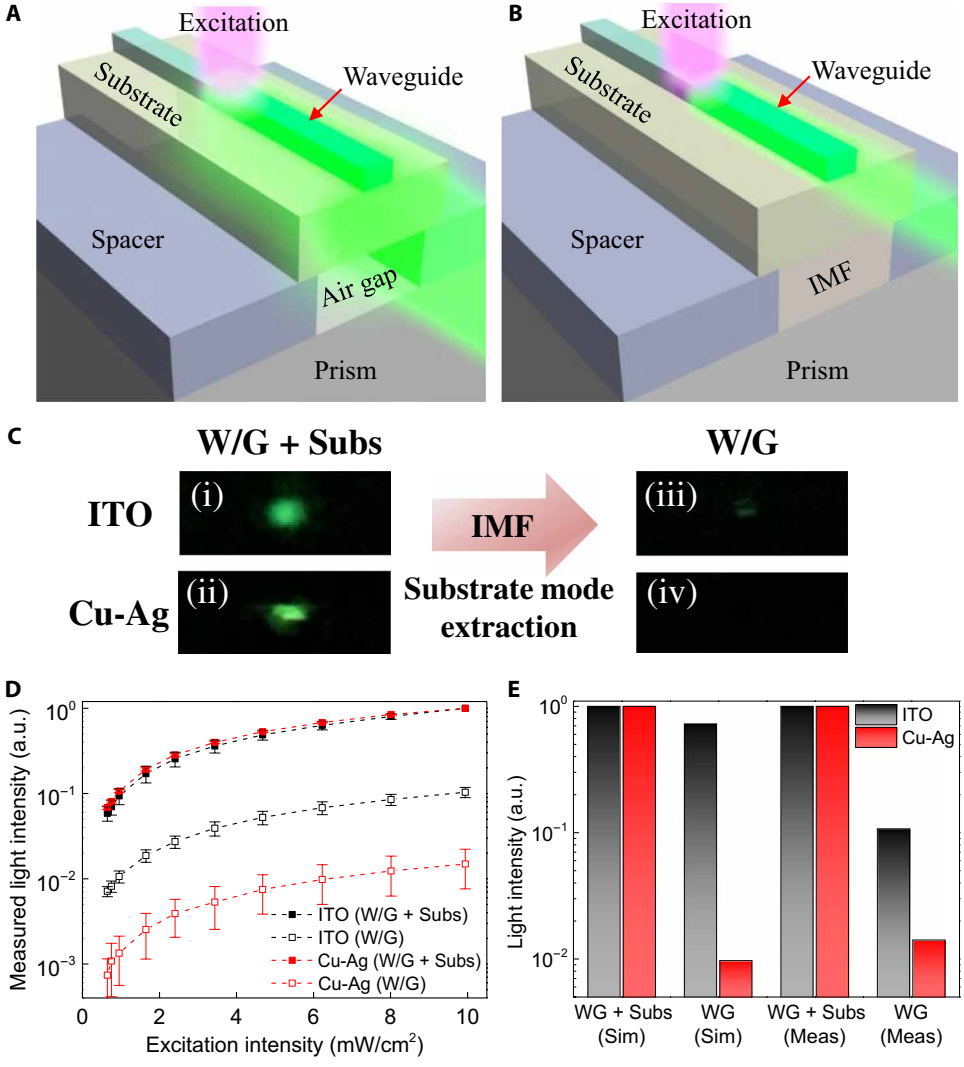

Fig. 5. Experimental investigation of waveguide mode elimination. 3D schematic illustrations of the experiment setup (**A**) with air and (**B**) with IMF under the sample substrate. The sample was placed on top of the spacers with a small gap away from the prism. The gap was filled with IMF to remove substrate mode from the sample. The fabricated stripe-patterned waveguide in this experiment consists of organic and anode layers without the top Al. (**C**) Photographs of the light detection from the ITO and Cu-Ag waveguide samples. Photographs of (i) ITO and (ii) Cu-Ag samples without IMF. Photographs of (iii) ITO and (iv) Cu-Ag samples with IMF. The waveguide mode was observed in the ITO sample but completely disappeared in the Cu-Ag sample, indicating no optical energy in the form of the waveguide mode. (**D**) Measured light intensities of ITO and Cu-Ag samples as a function of excitation light intensity, where the error bar represents 1 SD of three different samples. Measured light intensities were normalized with the maximum measured values without IMF in each sample. (**E**) Simulated and measured ratios of the waveguide mode. The ratio between the measured intensity with (W/G) and without IMF (W/G + Subs) was obtained. The intensity of W/G + Subs was normalized to unity in the bar plot.

introduces strong attenuation to the guided wave. The organic structure was redesigned since the TM_0 mode becomes pure dielectric mode without a thick metal cathode and requires a smaller cutoff thickness to be extracted. Both IMF and prism for the glass and fused silica substrates were used to remove substrate modes from the samples. Figure 5 (A and B) shows 3D schematic illustrations of the experiment setup with air gap and with IMF, respectively (see section S7 for more detail). The strip-line waveguide sample was placed on spacers consisting of two silicon pieces having a small gap underneath for IMF. A 405-nm laser was used to excite the EML of the waveguide line, and the mode intensity was measured at one end of the line. A bandpass filter with a bandwidth of 510 to 560 nm was used to measure the intensity of the emission that propagates through the waveguide strip while filtering out the 405-nm excitation light. The strip-line sample made on either ITO or Cu-Ag was measured with and without IMF to observe the intensity portion of the waveguide mode. The measured light intensity without IMF results from the sum of the waveguide and substrate modes. However, the use of IMF extracts the substrate mode, and the index-matched prism completely removes this extracted substrate mode out of the sample, leaving only the waveguide mode in the sample to be detected.

Figure 5C shows the photograph of a sample emission observed from the front side of the ITO and Cu-Ag samples with air gap and with IMF. Both samples showed distinct green emissions without IMF as shown in images (i) and (ii). When the substrate mode was removed by IMF, only the ITO sample showed the noticeable light at the end of the waveguide in image (iii), whereas no green light was observed from the Cu-Ag sample in image (iv), indicating that essentially, no light was guided in the waveguide.

Figure 5D shows the measured light intensities of the ITO and Cu-Ag samples as a function of excitation intensity, where the samples were normalized with the maximum intensity without IMF. Both waveguides showed similar values without IMF (filled squares), meaning that similar amounts of energies were delivered to the detector without IMF. The measured intensities of both samples were largely reduced when IMF was applied, and the measured intensity ratio with and without IMF of each sample was almost constant regardless of the excitation power, which is represented in Fig. 5E. The designed waveguide structure included a small portion of waveguide mode in the Cu-Ag device of ~1%, which was consistent with the measurement of 1.4%. However, the measured light intensities dropped to 10.7% of the original intensity for the ITO-based waveguide with IMF, showing that large amount of energy was still stored in the ITO waveguide.

MATERIALS AND METHODS

Calculation of spectral power distribution

Spectral Poynting vector in the propagation direction was first calculated in the OLED structure using dyadic Green's function with the dipole excitation. The Poynting vector was calculated as functions of both wavelength and $k_{||}/k_{EML}$, where air, glass, waveguide, or SPP mode can be found in the wave number range $0 < k_{||}/k_{EML} < k_{air}/k_{EML}$, $k_{air}/k_{EML} < k_{||}/k_{EML} < k_{glass}/k_{EML}$, $k_{glass}/k_{EML} < k_{||}/k_{EML} < 1$, or $1 < k_{||}/k_{EML}$, respectively. $k_{||}$ and k_{EML} are the wave numbers in horizontal direction and of the EML, respectively, where $k_{EML} = 2\pi n_{EML}/\lambda$. n_{EML} is the refractive index of CBP, and λ is the operating wavelength. $k_{air} = 2\pi/\lambda$ and $k_{glass} = 2\pi n_{glass}/\lambda$. The spectral power distribution shown in Fig. 2 (A and B) was obtained by integrating the spectral Poynting vector with respect to the corresponding $k_{||}/k_{EML}$ of each mode and normalizing to unity and that in Fig. 2 (C and D) was calculated by integrating the spectral power distribution over the entire wavelength range for each mode. The dipole source was placed at the center of the EML, and permittivity of each material was measured by spectroscopic ellipsometry. Dipole orientation factor of 0.77 was used with the assumption of $Ir(ppy)_2acac$ emitter (*54*), and its emission spectrum was integrated to obtain the spectral power distributions.

TCE film deposition and characterization

Materials used in this work were deposited by an evaporator from Angstrom Engineering (Evovac Evaporator, for Ge/Al) or a sputter deposition tool from Kurt J. Lesker Company (Lab 18, PVD-75, for Cu/Ag/ITO). Cu-Ag and ITO films were deposited at each optimal deposition rate that gives the highest transmittance and lowest resistivity (Cu/Ge/Al, Ag, and ITO deposition rates of 0.5, 3, and 1.7 Å/s, respectively). All the films were deposited using DC magnetron sputtering. Film thickness, optical constants, and transmission spectra were measured using spectroscopic ellipsometry method using J. A. Woollam Inc. (M-2000). The transmittance used in this work was the absolute transmission of the film including the substrate (not normalized over the substrate). The reflection spectra were obtained by a thin-film measurement instrument from Filmetrics (F20). Surface characterization was measured using atomic force microscopy using a Bruker ICON AFM under tapping mode. Electrical sheet resistance was calculated using a four-point probe method (FPP-5000, Miller Design & Equipment). Each sheet resistance was the average of three individual samples, with five independent measurements for each sample. A glass substrate (1.1 mm; purchased from Luminescence Technology Corporation) was used for Cu-Ag or bare Ag films.

OLED fabrication and characteristics

Commercial ITO-coated glass substrate purchased from Zhuhai Kaivo Optoelectronic Technology Co. Ltd. was used for the reference sample in this work. All organic semiconductors used in this work and a bare glass substrate for Cu-Ag OLEDs were purchased from Luminescence Technology Corporation. Bare glass and ITO-coated glass substrates were precleaned with acetone and isopropanol under sonication for 10 min before fabrication. Organic molecules were thermally evaporated as received without additional purification and deposited at rates of 0.2 to 1.0 Å/s under a base pressure less than 1×10^{-6} mbar. Cu-Ag anode was sputtered at a DC power of 100 W under sputtering pressure of 3 mtorr in the tool (Lab 18, PVD-75). Argon was used to strike plasma, and the base pressure of chamber was less than 1×10^{-6} torr. Three nanometers of aluminum-doped zinc oxide film was passivated on a Cu-Ag film using atomic layer deposition technique to prevent Ag diffusion. Top Al was purchased from Kurt J. Lesker Company and thermally evaporated with shadow mask to define a device area of 1 mm^2. Hewlett-Packard HP4156A parameter analyzer and Si photodiode FDS1010-CAL from Thorlabs were used to measure the current, voltage, and photocurrent of the OLEDs. Spectra of the OLEDs were measured using an Ocean Optics HR4000CG-UV-NIR spectrometer. Device EQEs and spectra were all measured in air without encapsulation.

Experiment setup and characterization of modal elimination

Fused silica substrate was purchased from University Wafer Inc. and used to measure waveguide mode elimination. Fused silica substrates

were precleaned with acetone and isopropanol under sonication for 10 min. The samples were moved to a thermal evaporator after the anode depositions in sputter (Lab 18, PVD-75). Kapton tape was used to define the line shape of waveguide, and the tape was removed before the measurement. Silicon pieces (0.5 mm) were used as holders as shown in Fig. 3A. IMF matched to refractive index of fused silica was used to extract substrate mode and thus measure the amount of energy confined in the waveguide, and a prism made of fused silica was used to completely remove the extracted substrate mode out of the system. IMF and fused silica were purchased from Cargille Laboratories and Thorlabs, respectively. Excitation laser source operating at 405 nm was purchased from Thorlabs, and an intensity range from 0.68 to 11.8 mW/cm^2 was used to excite the waveguide modes. Color filters purchased from Thorlabs were used to observe the waveguide modes. All the measurements were done in air without encapsulation.

SUPPLEMENTARY MATERIALS

Supplementary material for this article is available at http://advances.sciencemag.org/cgi/content/full/7/26/eabg0355/DC1

REFERENCES AND NOTES

1. A. B. Chwang, M. Hack, J. J. Brown, Flexible OLED display development: Strategy and status. *J. Soc. Inf. Display* **13**, 481–486 (2005).
2. M. H. Park, T. H. Han, Y. H. Kim, S. H. Jeong, Y. Lee, H. K. Seo, H. Cho, T. W. Lee, Flexible organic light-emitting diodes for solid-state lighting. *J. Photon Energy* **5**, 053599 (2015).
3. M. A. Baldo, D. F. O'Brien, Y. You, A. Shoustikov, S. Sibley, M. E. Thompson, S. R. Forrest, Highly efficient phosphorescent emission from organic electroluminescent devices. *Nature* **395**, 151–154 (1998).
4. H. Uoyama, K. Goushi, K. Shizu, H. Nomura, C. Adachi, Highly efficient organic light-emitting diodes from delayed fluorescence. *Nature* **492**, 234–238 (2012).
5. K. Hong, J. L. Lee, Review paper: Recent developments in light extraction technologies of organic light emitting diodes. *Electron. Mater. Lett.* **7**, 77–91 (2011).
6. W. Brütting, J. Frischeisen, T. D. Schmidt, B. J. Scholz, C. Mayr, Device efficiency of organic light-emitting diodes: Progress by improved light outcoupling. *Phys. Stat. Solidi* **210**, 44–65 (2013).
7. A. Salehi, X. Fu, D. H. Shin, F. So, Recent advances in OLED optical design. *Adv. Funct. Mater.* **29**, 1808803 (2019).
8. C.-Y. Lu, M. Jiao, W. K. Lee, C. Y. Chen, W. L. Tsai, C. Y. Lin, C. C. Wu, Achieving above 60% external quantum efficiency in organic light-emitting devices using ITO-free low-index transparent electrode and emitters with preferential horizontal emitting dipoles. *Adv. Funct. Mater.* **26**, 3250–3258 (2016).
9. T. Matsushima, F. Bencheikh, T. Komino, M. R. Leyden, A. S. D. Sandanayaka, C. Qin, C. Adachi, High performance from extraordinarily thick organic light-emitting diodes. *Nature* **572**, 502–506 (2019).
10. Y. Sun, S. R. Forrest, Enhanced light out-coupling of organic light-emitting devices using embedded low-index grids. *Nat. Photonics* **2**, 483–487 (2008).
11. S. Jeon, S. Lee, K. H. Han, H. Shin, K. H. Kim, J. H. Jeong, J. J. Kim, High-quality white OLEDs with comparable efficiencies to LEDs. *Adv. Opt. Mater.* **6**, 1701349 (2018).
12. W. H. Koo, S. M. Jeong, F. Araoka, K. Ishikawa, S. Nishimura, T. Toyooka, H. Takezoe, Light extraction from organic light-emitting diodes enhanced by spontaneously formed buckles. *Nat. Photonics* **4**, 222–226 (2010).
13. Y. Li, M. Kovačič, J. Westphalen, S. Oswald, Z. Ma, C. Hänisch, P. A. Will, L. Jiang, M. Junghaehnel, R. Scholz, S. Lenk, S. Reineke, Tailor-made nanostructures bridging chaos and order for highly efficient white organic light-emitting diodes. *Nat. Commun.* **10**, 2972 (2019).
14. B. R. Lee, E. D. Jung, J. S. Park, Y. S. Nam, S. H. Min, B. S. Kim, K. M. Lee, J. R. Jeong, R. H. Friend, J. S. Kim, S. O. Kim, M. H. Song, Highly efficient inverted polymer light-emitting diodes using surface modifications of ZnO layer. *Nat. Commun.* **5**, 4840 (2014).
15. T.-H. Han, Y. Lee, M. R. Choi, S. H. Woo, S. H. Bae, B. H. Hong, J. H. Ahn, T. W. Lee, Extremely efficient flexible organic light-emitting diodes with modified graphene anode. *Nat. Photonics* **6**, 105–110 (2012).
16. N. Li, S. Oida, G. S. Tulevski, S. J. Han, J. B. Hannon, D. K. Sadana, T. C. Chen, Efficient and bright organic light-emitting diodes on single-layer graphene electrodes. *Nat. Commun.* **4**, 2294 (2013).
17. J. Lee, T. H. Han, M. H. Park, D. Y. Jung, J. Seo, H. K. Seo, H. Cho, E. Kim, J. Chung, S. Y. Choi, T. S. Kim, T. W. Lee, S. Yoo, Synergetic electrode architecture for efficient graphene-based flexible organic light-emitting diodes. *Nat. Commun.* **7**, 11791 (2016).
18. Y.-H. Huang, C. Y. Lu, S. T. Tsai, Y. T. Tsai, C. Y. Chen, W. L. Tsai, C. Y. Lin, H. W. Chang, W. K. Lee, M. Jiao, C. C. Wu, Enhancing light out-coupling of organic light-emitting devices using indium tin oxide-free low-index transparent electrodes. *Appl. Phys. Lett.* **104**, 183302 (2014).
19. H.-W. Chang, Y. H. Kim, J. Lee, S. Hofmann, B. Lüssem, L. Müller-Kamp, M. C. Gather, K. Leo, C.-C. Wu, Color-stable, ITO-free white organic light-emitting diodes with enhanced efficiency using solution-processed transparent electrodes and optical outcoupling layers. *Org. Electron.* **15**, 1028–1034 (2014).
20. Y.-H. Ho, K. Y. Chen, S. W. Liu, Y. T. Chang, D. W. Huang, P. K. Wei, Transparent and conductive metallic electrodes fabricated by using nanosphere lithography. *Org. Electron.* **12**, 961–965 (2011).
21. Y. G. Bi, J. Feng, J. H. Ji, Y. Chen, Y. S. Liu, Y. F. Li, Y. F. Liu, X. L. Zhang, H. B. Sun, Ultrathin and ultrasmooth Au films as transparent electrodes in ITO-free organic light-emitting devices. *Nanoscale* **8**, 10010–10015 (2016).
22. C. Zhang, Q. Huang, Q. Cui, C. Ji, Z. Zhang, X. Chen, T. George, S. Zhao, L. J. Guo, High-performance large-scale flexible optoelectronics using ultrathin silver films with tunable properties. *ACS Appl. Mater. Interfaces* **11**, 27216–27225 (2019).
23. J. Ouyang, C. W. Chu, F. C. Chen, Q. Xu, Y. Yang, High-conductivity poly(3,4-ethylenedioxy thiophene):poly(styrene sulfonate) film and its application in polymer optoelectronic devices. *Adv. Funct. Mater.* **15**, 203–208 (2005).
24. Y. H. Kim, C. Sachse, M. L. Machala, C. May, L. Müller-Meskamp, K. Leo, Highly conductive PEDOT:PSS electrode with optimized solvent and thermal post-treatment for ITO-free organic solar cells. *Adv. Funct. Mater.* **21**, 1076–1081 (2011).
25. Y. G. Bi, Y. F. Liu, X. L. Zhang, D. Yin, W. Q. Wang, J. Feng, H. B. Sun, Ultrathin metal films as the transparent electrode in ITO-free organic optoelectronic devices. *Adv. Opt. Mater.* **7**, 1800778 (2019).
26. M. Morales-Masis, S. De Wolf, R. Woods-Robinson, J. W. Ager, C. Ballif, Transparent electrodes for efficient optoelectronics. *Adv. Electron. Mater.* **3**, 1800778 (2017).
27. W. den Boer, G. S. Smith, Dual select diode AMLCDs: A path towards scalable two-mask array designs. *J. Soc. Inf. Display.* **13**, 199–204 (2005).
28. C. Jeong, Y.-b. Park, L. J. Guo, Enahnced light outcoupling from OLEDs by suppressing guided modes formation using an ultrathin flexible transparent conductor, in *2020 IEEE International Electron Devices Meeting (IEDM, Virtual)*, 12 to 18 December 2020.
29. J. Wu, M. Agrawal, H. A. Becerril, Z. Bao, Z. Liu, Y. Chen, P. Peumans, Organic light-emitting diodes on solution-processed graphene transparent electrodes. *ACS Nano* **4**, 43–48 (2010).
30. H. J. Peng, X. L. Zhu, J. X. Sun, X. M. Yu, M. Wong, H. S. Kwok, Efficiency improvement of phosphorescent organic light-emitting diodes using semitransparent Ag as anode. *Appl. Phys. Lett.* **88**, 033509 (2006).
31. C. Cho, B. Zhao, G. D. Tainter, J. Y. Lee, R. H. Friend, D. di, F. Deschler, N. C. Greenham, The role of photon recycling in perovskite light-emitting diodes. *Nat. Commun.* **11**, 611 (2020).
32. Y. Shirasaki, G. J. Supran, M. G. Bawendi, V. Bulović, Emergence of colloidal quantum-dot light-emitting technologies. *Nat. Photonics* **7**, 13–23 (2012).
33. J. J. Wierer, A. David, M. M. Megens, III-nitride photonic-crystal light-emitting diodes with high extraction efficiency. *Nat. Photonics* **3**, 163–169 (2009).
34. J. N. Polky, G. L. Mitchell, Metal-clad planar dielectric waveguide for integrated optics. *J. Opt. Soc. Am.* **64**, 274–279 (1974).
35. Y. F. Li, J. W. Y. Lit, General formulas for the guiding properties of a multilayer slab wave-guide. *J. Opt. Soc. Am. A* **4**, 671–677 (1987).
36. J. A. Dionne, L. A. Sweatlock, H. A. Atwater, A. Polman, Plasmon slot waveguides: Towards chip-scale propagation with subwavelength-scale localization. *Phys. Rev. B* **73**, 035407 (2006).
37. S. A. Maier, SpringerLink (Online service), *Plasmonics: Fundamentals and Applications* (Springer, 2007), p. xxiv, 223 p.
38. K. Celebi, T. D. Heidel, M. A. Baldo, Simplified calculation of dipole energy transport in a multilayer stack using dyadic Green's functions. *Opt. Express* **15**, 1762–1772 (2007).
39. P. S. Neelakanta, *Handbook of Electromagnetic Materials: Monolithic and Composite Versions and their Applications* (CRC Press, 1995), p. 591.
40. A. Anders, E. Byon, D.-H. Kim, K. Fukuda, S. H. N. Lim, Smoothing of ultrathin silver films by transition metal seeding. *Solid State Commun.* **140**, 225–229 (2006).
41. L. Vj, N. P. Kobayashi, M. Saif Islam, W. Wu, P. Chaturvedi, N. X. Fang, S. Y. Wang, R. Stanley Williams, Ultrasmooth silver thin films deposited with a germanium nucleation layer. *Nano Lett.* **9**, 178–182 (2009).
42. W. Chen, M. D. Thoreson, S. Ishii, A. V. Kildishev, V. M. Shalaev, Ultra-thin ultra-smooth and low-loss silver films on a germanium wetting layer. *Opt. Express* **18**, 5124–5134 (2010).
43. N. Formica, D. S. Ghosh, A. Carrilero, T. L. Chen, R. E. Simpson, V. Pruneri, Ultrastable and atomically smooth ultrathin silver films grown on a copper seed layer. *ACS Appl. Mater. Interfaces* **5**, 3048–3053 (2013).
44. C. Zhang, C. Ji, Y.-B. Park, L. J. Guo, Thin-metal-film-based transparent conductors: Material preparation, optical design, and device applications. *Adv. Opt. Mater.* **9**, 2001298 (2020).

45. G. Haacke, New figure of merit for transparent conductors. *J. Appl. Phys.* **47**, 4086–4089 (1976).
46. H. Askari, H. Fallah, M. Askari, M. Charkhchi Mohmmadieyh, Electrical and optical properties of ITO thin films prepared by DC magnetron sputtering for low-emitting coatings. arXiv:1409.5293 [cond-mat.mtrl-sci] (18 September 2014).
47. S. J. Byrnes, Multilayer optical calculations. arXiv:1603.02720 [physics.comp-ph] (6 March 2016).
48. A. K. Kulkarni, K. H. Schulz, T. S. Lim, M. Khan, Dependence of the sheet resistance of indium-tin-oxide thin films on grain size and grain orientation determined from x-ray diffraction techniques. *Thin Solid Films* **345**, 273–277 (1999).
49. M. G. Helander, Z. B. Wang, J. Qiu, M. T. Greiner, D. P. Puzzo, Z. W. Liu, Z. H. Lu, Chlorinated indium tin oxide electrodes with high work function for organic device compatibility. *Science* **332**, 944–947 (2011).
50. M. A. Baldo, C. Adachi, S. R. Forrest, Transient analysis of organic electrophosphorescence. II. Transient analysis of triplet-triplet annihilation. *Phys. Rev. B* **62**, 10967–10977 (2000).
51. S. Reineke, K. Walzer, K. Leo, Triplet-exciton quenching in organic phosphorescent light-emitting diodes with Ir-based emitters. *Phys. Rev. B* **75**, 125328 (2007).
52. Y. Sun, S. R. Forrest, Organic light emitting devices with enhanced outcoupling via microlenses fabricated by imprint lithography. *J. Appl. Phys.* **100**, 073106 (2006).
53. Y. Qu, J. Kim, C. Coburn, S. R. Forrest, Efficient, nonintrusive outcoupling in organic light emitting devices using embedded microlens arrays. *ACS Photonics* **5**, 2453–2458 (2018).
54. S.-Y. Kim, W.-I. Jeong, C. Mayr, Y.-S. Park, K.-H. Kim, J.-H. Lee, C.-K. Moon, W. Brütting, J.-J. Kim, Organic light-emitting diodes with 30% external quantum efficiency based on a horizontally oriented emitter. *Adv. Funct. Mater.* **23**, 3896–3900 (2013).
55. S. Jeong, S. Jung, H. Kang, D. Lee, S.-B. Choi, S. Kim, B. Park, K. Yu, J. Lee, K. Lee, Role of polymeric metal nucleation inducers in fabricating large-area, flexible, and transparent electrodes for printable electronics. *Adv. Funct. Mater.* **27**, 1606842 (2017).
56. P. Melpignano, C. Cioarec, R. Clergereaux, N. Gherardi, C. Villeneuve, L. Datas, E-beam deposited ultra-smooth silver thin film on glass with different nucleation layers: An optimization study for OLED micro-cavity application. *Org. Electron.* **11**, 1111–1119 (2010).
57. E. G. Seebauer, C. E. Allen, Estimating surface-diffusion coefficients. *Prog. Surf. Sci.* **49**, 265–330 (1995).
58. H. C. Kim, T. L. Alford, D. R. Allee, Thickness dependence on the thermal stability of silver thin films. *Appl. Phys. Lett.* **81**, 4287–4289 (2002).
59. A. Ciesielski, L. Skowronski, E. Górecka, J. Kierdaszuk, T. Szoplik, Growth model and structure evolution of Ag layers deposited on Ge films. *Beilstein J. Nanotechnol.* **9**, 66–76 (2018).
60. D. Gu, C. Zhang, Y. K. Wu, L. J. Guo, Ultrasmooth and thermally stable silver-based thin films with subnanometer roughness by aluminum doping. *ACS Nano* **8**, 10343–10351 (2014).
61. W. M. Abbott, C. P. Murray, C. Zhong, C. Smith, C. McGuinness, E. Rezvani, C. Downing, D. Daly, A. K. Petford-Long, F. Bello, D. McCloskey, J. F. Donegan, Less is more: Improved thermal stability and plasmonic response in Au films via the use of subnanometer Ti adhesion layers. *ACS Appl. Mater. Interfaces* **11**, 7607–7614 (2019).
62. M. Hovel, B. Gompf, M. Dressel, Dielectric properties of ultrathin metal films around the percolation threshold. *Phys. Rev. B* **81**, 035402 (2010).
63. E. H. Sondheimer, The mean free path of electrons in metals. *Adv. Phys.* **1**, 1–42 (1952).
64. D. Gall, Electron mean free path in elemental metals. *J. Appl. Phys.* **119**, 085101 (2016).
65. J. M. Camacho, A. I. Oliva, Surface and grain boundary contributions in the electrical resistivity of metallic nanofilms. *Thin Solid Films* **515**, 1881–1885 (2006).
66. A. F. Mayadas, M. Shatzkes, J. F. Janak, Electrical resistivity model for polycrystalline films: The case of specular reflection at external surfaces. *Appl. Phys. Lett.* **14**, 345–347 (1969).
67. K. N. Tu, A. M. Gusak, I. Sobchenko, Linear rate of grain growth in thin films during deposition. *Phys. Rev. B* **67**, 245408 (2003).
68. T. A. F. König, P. A. Ledin, J. Kerszulis, M. A. Mahmoud, M. A. El-Sayed, J. R. Reynolds, V. V. Tsukruk, Electrically tunable plasmonic behavior of nanocube–polymer nanomaterials induced by a redox-active electrochromic polymer. *ACS Nano* **8**, 6182–6192 (2014).
69. P. B. Johnson, R. W. Christy, Optical constants of the noble metals. *Phys. Rev. B* **6**, 4370–4379 (1972).

Acknowledgments

Funding: This work was supported in part by Zenithnano Tech. Ltd. and was performed in part at the University of Michigan Lurie Nanofabrication Facility. **Author contributions:** C.J. conducted OLED fabrication and test. Y.-B.P. fabricated and characterized ultrathin smooth Ag alloy films. L.J.G. advised and supported the project. **Competing interests:** L.J.G. declares financial interest in Zenithnano Tech. Ltd. **Data and materials availability:** All data needed to evaluate the conclusions in the paper are present in the paper and/or the Supplementary Materials. Additional data related to this paper may be requested from the authors.

Submitted 7 December 2020
Accepted 13 May 2021
Published 25 June 2021
10.1126/sciadv.abg0355

Citation: C. Jeong, Y.-B. Park, L. J. Guo, Tackling light trapping in organic light-emitting diodes by complete elimination of waveguide modes. *Sci. Adv.* **7**, eabg0355 (2021).